

The influence of isolated observations on short-range numerical weather forecasts

By ERLAND KÄLLÉN and XIANG-YU HUANG, *Department of Meteorology,* University of Stockholm, Arrhenius Laboratory, S-106 91 Stockholm, Sweden*

(Manuscript received 10 August 1987; in final form 7 December 1987)

ABSTRACT

The influence of isolated observations on short-range numerical weather forecasts has been studied by comparing ECMWF forecasts over limited areas. We first identify situations where a single observation has a large impact on the analysis and then study the subsequent error growth by comparing 2 numerical forecasts with and without the observation. The study is carried out in data-sparse regions. We have analysed 152 cases and the results show a large spread in the perturbation growth rates which are calculated as the RMS differences between forecasted (up to 48 h) 500 mb geopotential heights. The average growth rate is close to earlier estimates of error growths, but this growth rate is not very representative for the ensemble of forecasts which have been investigated. Instead, there is a tendency towards a bimodal distribution, with either very rapid or slow perturbation growth rates. To identify the physical cause of this large variation in growth rates, we have evaluated local instability indexes for each case and compared these with the actual growth rates. The instability index is calculated from both the baroclinic and barotropic properties of the unperturbed, initial flow fields. We find that the occurrence of rapid perturbation growth rates seems to be coupled to the baroclinicity of the flow in the vicinity of the localized perturbation. Barotropic effects in terms of strong, local vorticity gradients do not seem to be associated with rapid perturbation growths.

1. Introduction

The predictability problem in numerical weather prediction has received considerable attention ever since the first efforts in this field were made in the 1950s. One of the pioneering authors was Thompson (1957) who outlined the basic problem of how uncertainties in the initial state would lead to errors in the forecast. Thompson (1957) also described a method by which the predictability of a certain flow situation could be assessed. This method involved the calculation of vorticity gradients in the vertically-averaged and vertically-sheared flow. Thompson (1957) proposed that his theory could be used to give error bounds on a forecast in a particular flow situa-

tion. However, he did not show any actual calculations of the predictability measures from operational numerical forecasts. To our knowledge, this type of predictability study has not been pursued since the work of Thompson (1957).

Instead, predictability theory has advanced mainly through the work of Lorenz (1963, 1969, 1982) and others who have taken a more global view of the problem. Predictability has been discussed in terms of statistical averages for an ensemble of forecasts over a global or hemispheric domain. Though a spectral analysis of two-dimensional flow, Lorenz (1969) showed that the ultimate deterministic predictability of the atmosphere is limited to around 2 weeks. More recent work by Arpe et al. (1985) with the ECMWF operational forecasting system demonstrates that at present, the practical predictability time is limited to around 7 days. In another

* Contribution no 575.

ECMWF model study, Lorenz (1982) investigates error growth rates both as a function of error amplitude and forecasting time. Lorenz (1982) also attempts to separate the influence from analysis errors and that from model errors. When 2 model runs with different initial conditions are compared and it is assumed that the model is "perfect", one may calculate a perturbation doubling time. This doubling time is very much dependent on the perturbation amplitude according to Lorenz (1982). Another factor which also must influence the perturbation growth rate is the initial flow state. This aspect is discussed by Thompson (1957) who deals with the initial error growth for a particular flow situation rather than the average error growth for an ensemble of forecasts over a large domain. For some particular forecasts, this aspect of predictability theory was considered by Hollingsworth et al. (1985). In a recent study, Dalcher and Kalnay (1987) extended the Lorenz (1982) study to the wavenumber domain, thereby studying the predictability of different scales of motion. This approach again takes a global rather than a local view of the predictability problem.

In this study, we will attempt to combine the approaches of Thompson (1957) and Lorenz (1982) by computing localized initial perturbation growths for particular flow situations using forecasting data from the ECMWF model. The localized perturbations will be found through a procedure which identifies situations where a single, isolated surface pressure observation has a large impact on the initial state of a numerical forecast run. By comparing this forecast run with the forecast from the previous day, where the observation was absent, we are able to calculate the growth of an isolated perturbation by only using archived forecasts. Situations with isolated surface pressure observations frequently occur in the southern hemisphere and an example of a case which demonstrates the drastic impact that an isolated observation may have, was given by Cats (1984). In our study, 152 cases will be investigated and we will examine the overall statistical properties of the data set. The average perturbation growth rate will turn out to agree closely with the results of Lorenz (1982), but there is a considerable variation in the perturbation growth rates for different flow situations. The question then arises of how representative the

averaged perturbation growth rate actually is for a given weather situation?

Following the ideas of Thompson (1957), we proceed to calculate localized perturbation growth indexes for the initial states of our data set. We separate baroclinic and barotropic processes when calculating the growth index, thus trying to evaluate the relative importance of the 2 mechanisms. The baroclinic growth index is determined through standard, linear baroclinic instability theory (Holton, 1979) while the barotropic index is calculated following the procedure of Thompson (1986). By comparing the predicted growth rate with the actual perturbation growth rate, we can assess the usefulness of a growth index. We also suggest a possibility of using a growth index to improve the data analysis which determines the initial state of a forecast.

The manuscript is organized as follows. In Section 2, the data analysis along with some statistical properties of the data set is presented. Section 3 deals with localized baroclinic instability, while Section 4 addresses the localized barotropic instability. In Section 5, we finally draw some conclusions regarding the applicability of our results to meteorological data analysis.

2. Analysis method

To investigate the impact of isolated observations, we first want to identify cases where a single observation has a large and localized influence on the initial conditions for a forecast run. We also wish to compare this run with another run where the perturbation is absent. This could be done by setting up a series of experiments with simulated forecast runs, but in order to obtain statistically significant results, we would have to choose a large sample of initial states and such a computer experiment would be very expensive. Instead we attempt to use operational forecast runs from ECMWF, where we have singled out cases which contain localized perturbations due to isolated observations. The unperturbed forecast runs are obtained using forecasts from the previous day if we know that the particular observation is absent.

To be sure that we deal with isolated observations we only examine data in the southern

hemisphere oceanic areas south of 40°S. Over the southern hemisphere, oceanic observations are scarce and the initial state for a forecast is mainly a reflection of a previous 6-hour forecast run (ECMWF, 1985). If an observation comes in, it may, however, give a large and localized impact on the analysis which is what we are looking for in this study. We therefore monitor the difference between the first guess field, which comes from a previous forecast run, and the initialized fields at the position of an observation. The initialized fields are used as an initial state for a forecast run (ECMWF, 1985). As we wish the observation to be as influential as possible, we only look at surface pressure observations. The localized impact of such an observation will normally have an equivalent barotropic structure in the vertical (Cats, 1984). We therefore obtain a perturbation which influences the initial state at all levels. In addition, we know that surface pressure observations are often collocated with radiosonde stations, which further enhances the vertical coherence of the impact.

To identify isolated observations, we make use of the box structure of the ECMWF analysis scheme. Observations are analyzed separately within each box, which has a horizontal size of about 660×660 km (ECMWF, 1985). We only pick situations where an analysis box contains a single surface pressure observation. This situation is quite usual in the southern hemisphere. If 2 additional criteria are fulfilled, the situation is selected as a case. The 2 criteria are:

(1) the difference between the first guess and initialized 1000 hPa height at the position of the observation exceeds 50 m;

(2) the first guess and initialized 1000 hPa heights are identical the day before the observation took place (i.e., the observation was absent the previous day).

With these criteria, we select cases from 16 months of operational ECMWF analysis and observational data. Totally, we have obtained 152 cases and these cases have been subdivided into winter and summer cases. We have only examined typical winter months (April–August) and summer months (October–February).

For each case, we then compare 2 forecasts from subsequent days which check at the same point in time (Fig. 1). The comparison is made at the 500 hPa level over an area which extends 90°

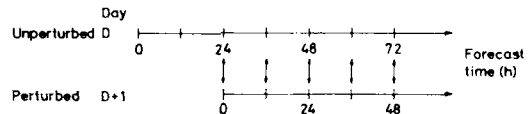


Fig. 1. Data structure when comparing 2 forecasts from 2 consecutive days. Differences are calculated for forecasts checking at the same point in time (vertical arrows).

in longitude and 45° in latitude. The area is positioned to include the influential observation in the western half, thus allowing for downstream propagation of the disturbance in a mean westerly flow. An example of such a comparison is shown in Fig. 2. The isolated observation gives rise to a perturbation of 50 m in the upper, left half of the area and as the forecast evolves in time, we see an eastward propagation of the disturbance. Simultaneously, we also observe a strong amplification of the perturbation, i.e., the 2 forecasts will gradually diverge within this area. The initial perturbation increases by a factor of 4 during the 48-h time interval shown in Fig. 2 and the isolated observation thus had a very strong impact on the forecast. Which forecast that corresponds best to reality is impossible to say as observations are scarce in this region (South Pacific Ocean). We can only conclude that the 2 forecasts are markedly different.

Another example of a localized perturbation is also seen in Fig. 2a, in the lower right half part of the figure. We see a localized perturbation with an amplitude of 100 m. This perturbation is advected out of the area shown in Fig. 2, but it turns out (not shown here) that this perturbation actually decreases in time and the 2 forecasts converge in an area downstream of the one shown in Fig. 2. We thus see that in a particular weather situation, 2 perturbations have widely different time evolutions which do not seem to be coupled to their initial amplitude.

This case only serves to illustrate the type of behaviour we wish to examine; to be able to draw any conclusions, we must analyze all of the 152 cases which we have selected. For this analysis, we choose to calculate the RMS difference between the 500 hPa heights of the 2 forecasts within the given area. We furthermore normalize the RMS difference by its initial value. We thus obtain a measure by which all of the cases can be

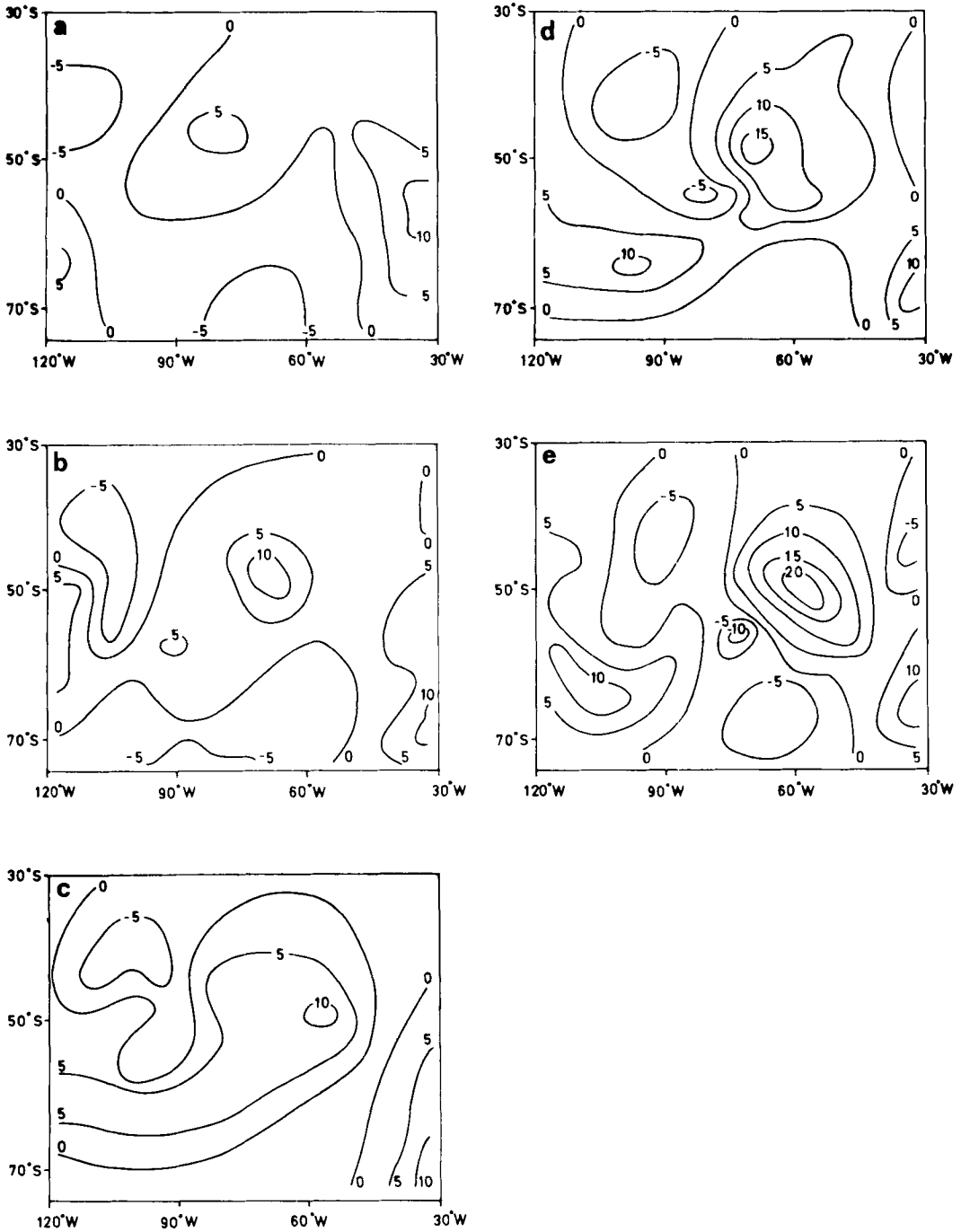


Fig. 2. Difference fields for 2 forecasts at the 500 hPa level. Contour lines are drawn at 50 m intervals and the labels are given in dekameters. The geographical position of the area is given in terms of latitude and longitude and the figures correspond to the following forecast times of the perturbed forecasts: (a) 0 h, (b) 12 h, (c) 24 h, (d) 36 h, (e) 48 h.

compared. The normalized RMS difference as a function of time for all cases is shown in Fig. 3, and we see that there is a large spread in the behaviour. By separating cases where the difference increases by more or less than a factor of 2, we obtain the 2 graphs shown in the right-hand part of Fig. 3. We find that in a large number of cases (about 15% of the total), the difference more than doubles in 48 h.

We may compare these results to the study of the ECMWF model error evolution of Lorenz (1982). Lorenz investigated the ECMWF model error behaviour when 2 model simulations from different initial states were compared. By computing an average of all the curves shown in Fig. 3, we obtain an average growth factor of 1.5 over 48 h (Fig. 4). To compare this with the Lorenz (1982) results, we must also know the characteristic amplitude of the initial perturbation. A frequency plot of the initial deviations is given in Fig. 5 and by computing an average over all our cases, we find that our initial RMS difference over the given area amounts to 42.7 m. From Fig. 1 in Lorenz (1982), we find that for an RMS difference of 40 m, the curves corresponding to model-model comparisons (thin curves) yield an error doubling time of around 4 days. Our

average result thus closely agrees with the findings of Lorenz (1982). Our Fig. 5 also shows the distribution of initial perturbations and we see that in some cases, the initial difference is so large that we will get reduced growth rates due to saturation effects. There are, however, no cases with an RMS difference below 19 m and thus the doubling time for small errors given by Lorenz (1982) (2.5 days) does not apply to this study. Moreover, the doubling time for small errors is only an extrapolated measure of error growth, which is very sensitive to the extrapolation method used (Dalcher and Kalnay, 1987). The values for perturbation growth at finite amplitudes (20–100 m) is more reliable, as it can be directly calculated from the data.

If we look at the average of all the cases which more than double the difference, we of course, observe a much more rapid average growth, while an average over all the other cases shows a considerably more gentle growth rate. By closely examining the diagram in Fig. 3, which shows the result for all cases, we see that there are 2 broad bands along which most curves seem to lie. Outside these 2 bands, which appear as darkened areas in Fig. 3, we have a lower curve density. This feature points towards a bimodality in the

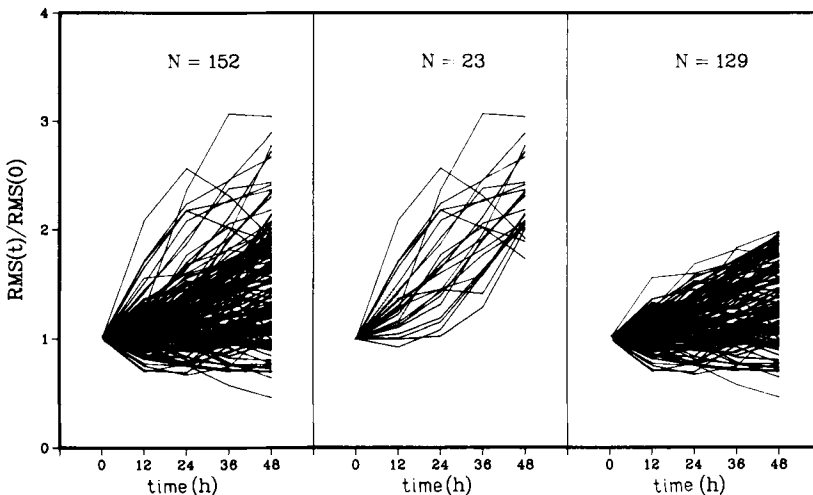


Fig. 3. Relative RMS difference as a function of forecast time for all the cases examined. The time periods used are the months April–August (winter) in 1984 and 1985 and the months October–February (summer) in 1984/85 and 1985/86. The two right-hand plots show the same curves as the left-hand plot, but the cases have been split into classes where the perturbation increases more (middle plot) or less (rightmost plot) than a factor of 2.

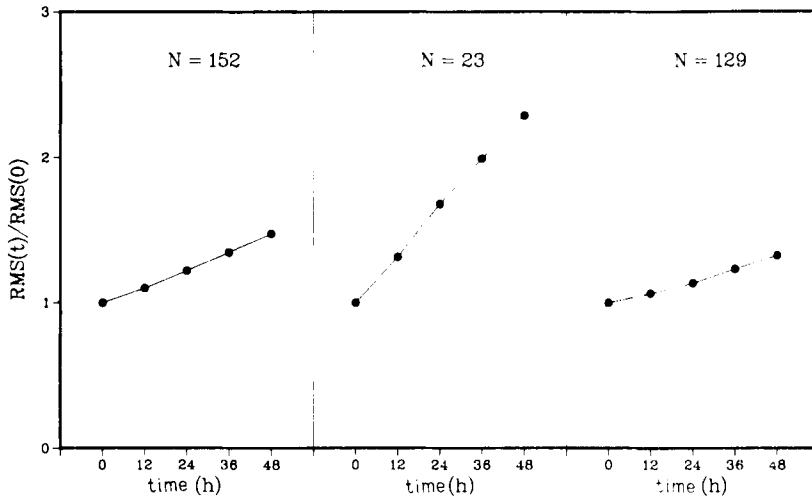


Fig. 4. Same as in Fig. 3, but here the average growth curve is shown.

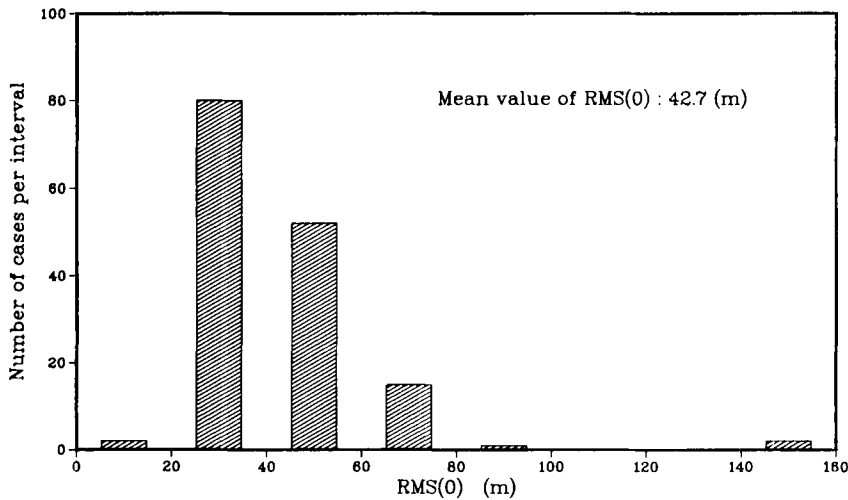


Fig. 5. Distribution of initial RMS differences in the 152 cases considered. The average value is 42.7 m and the spread is between a minimum value of 19.25 m and a maximum value of 150.95 m.

results and we will further investigate this by constructing frequency histograms for different forecast times.

We may further subdivide the cases into relative RMS growth classes and display the result in terms of a histogram. This is done in Fig. 6, where histograms of the number of cases within each growth class for summer and winter months separately is shown at different forecast times.

The RMS ratio is here plotted on a logarithmic scale and the histogram classes are equally spaced on the logarithmic scale. The diagrams apply to 12 and 48 h of forecast time; if we would have plotted a similar graph for 0 h of forecast time, all cases would have been in the class containing a logarithmic RMS ratio of zero units. As the forecast time evolves, the distribution spreads out into something which at first looks like a

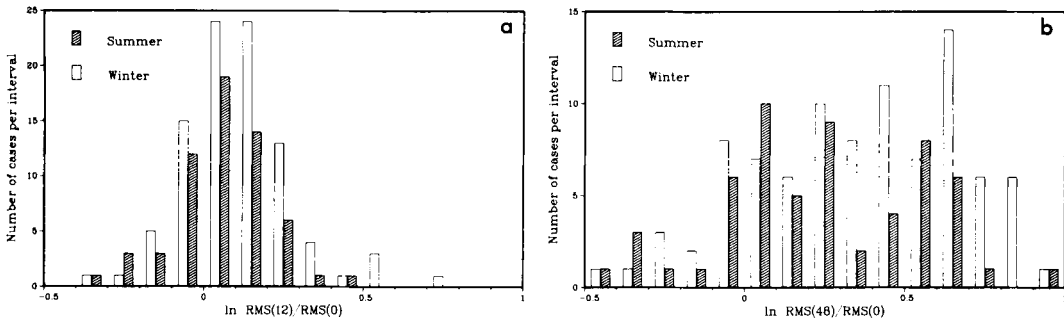


Fig. 6. Histogram of perturbation growth rates at 2 different forecast times. Summer and winter cases are separated. (a) 12 h of forecast time. (b) 48 h of forecast time.

Gaussian distribution. At 48 h, the distribution is, however, not very Gaussian; instead we observe a tendency towards a bimodal distribution, in particular for the summer cases (Fig. 6b). The bimodality of the data is of course difficult to assess due to the limited number of cases in the summer sample. We can, however, conclude that the distribution is no longer Gaussian at 48 h of forecast time, and that at least in the summer sample, there is a tendency towards a bimodality. In the winter sample, there is no apparent bimodality at 48 h, but at 36 h (not shown), there is also some sign of a bimodal distribution.

The minimum of the summer bimodal distribution corresponds to a doubling time of approximately 4 days. From this we conclude that the average doubling time is not very representative for a particular flow situation. Instead we find that either we have a moderate growth of the difference or there will be a very strong growth. The situation with an intermediate growth is less frequent. Examples of this tendency are illustrated by the 2 perturbations in Fig. 2 which have markedly different behaviours. As these 2 perturbations occur in the same flow situation, one is led to the conclusion that some local property of the flow, rather than any large-scale properties or size of the perturbation, determines whether the initial disturbance will grow or decay. The histogram in Fig. 6 also shows marked differences between summer and winter. Many more cases in winter than in summer show a rapid growth, but the cases where we see an extreme growth rate occur both in winter and in summer.

All this points to an instability mechanism which is localized in space and which occurs more frequently in winter than in summer. A possible candidate is local baroclinic instability and in Section 3, we will explore this further by computing a baroclinic growth index of the initial state.

3. Local baroclinic instability

In recent years, many studies have attempted to determine the localized properties of baroclinic instability. Frederiksen (1983) has demonstrated how the main cyclogenetic regions can be found by determining linear eigenmodes from a time-averaged, spatially varying flow state. It appears that regions of enhanced thermal wind gradients are efficient generators of baroclinic wave activity. The waves propagate downstream out of the generating region and eventually disperse and dissipate over a large area. Pierrehumbert (1984) has demonstrated how this phenomenon can be understood in an even simpler model and in particular he distinguishes between absolute versus convective instability. Absolute instability is defined as instability for a fixed point in space while convective instability implies that the wave grows in a coordinate system moving with the group velocity of the wave packet. If a region of enhanced thermal winds is fixed in space while a baroclinic wave packet propagates with a certain speed, the wave will only grow when it is inside the baroclinically active region. The instability of the wave packet thus depends on both the

thermal wind gradient and the propagation speed of the disturbance.

When determining eigenmodes from a time-averaged flow state, the difference between absolute and convective instability will be very noticeable as the regions of strong baroclinicity are fixed in space. In a particular flow state, the difference may not be so large, because here the regions of enhanced thermal wind will also be moving with the mean flow. This is particularly true over oceanic areas where the flow temperature gradients are not coupled to thermal contrasts at the surface. For waves with a relatively short wave-length (order Rossby's radius of deformation) the β -effect is negligible and the wave packets will travel with the speed of the mean flow. In this case, the waves will always be convectively unstable if the thermal gradients are nonzero in a domain enclosing the initial wave packet.

Relating the theories of localized baroclinic instability to our study of localized perturbation growth we hypothesize as follows. *If a localized perturbation in the analysis falls within an area of enhanced thermal winds in the first guess field, the perturbation growth will intensify.*

We will test this hypothesis by computing a local baroclinic growth index based on the local thermal wind, static stability and the Coriolis parameter. The connection between the growth index and the actual perturbation growth in the forecast will be investigated by constructing a scatter diagram. In order to apply linear theory, we only determine the perturbation growth during the first 12 h of the forecast.

The baroclinic growth index is computed by using standard normal mode, quasi-geostrophic baroclinic instability theory. From Holton (1979), we find the following standard equations governing the dynamics of a 2-layer, quasi-geostrophic model,

$$\begin{aligned} \frac{\hat{c}}{\hat{c}t} \nabla^2 \Psi &= -J(\Psi, \nabla^2 \Psi + f_0) - J(\tau, \nabla^2 \Psi), \\ \frac{\hat{c}}{\hat{c}t} (\nabla^2 - 2\lambda^2) \tau &= -J(\Psi, \nabla^2 \tau) \\ &\quad - J(\tau, \nabla^2 \Psi + f_0) + 2\lambda^2 J(\Psi, \tau), \end{aligned} \quad (1)$$

where $\Psi = (\Psi_1 + \Psi_3)/2$ and $\tau = (\Psi_1 - \Psi_3)/2$. The upper level is indicated by index 1, the lower level by index 3. The parameter $\lambda^2 = f_0/(\sigma \Delta p^2)$,

where $\sigma = -(\sigma/\theta)\hat{c}\theta/\hat{c}p$ is the ordinary static stability parameter and Δp is the pressure difference between the 2 layers. As we wish to investigate localized baroclinic instability, we disregard the β -effect ($f = f_0$).

We seek normal mode solutions of eq. (1) around a basic state which has a mean wind ($U, 0$) and a thermal wind (U_T, V_T). Note that we do not require the mean wind to be parallel to the thermal wind, which implies that we may have thermal advection in the basic state. When seeking normal mode solutions, we implicitly assume that the tendency induced by this thermal advection is small compared with the growth rate of a possibly unstable disturbance. This is necessary in order to be able to linearize around the basic state in a meaningful way. By assuming wave solutions in a periodic domain, where U, U_T and V_T are constant, we obtain the following form of the mean streamfunction Ψ and the thermal field τ :

$$\Psi = \hat{\Psi} e^{i(kx+ly-\omega t)} - Uy, \quad (2)$$

$$\tau = \hat{\tau} e^{i(kx+ly-\omega t)} - U_T y + V_T x,$$

and through an insertion into eqs. (1), we find the following dispersion relation:

$$\begin{aligned} \omega &= Uk + |kU_T + lV_T| \\ &\quad \times \sqrt{(k^2 + l^2 - 2\lambda^2)/(k^2 + l^2 + 2\lambda^2)} \end{aligned} \quad (3)$$

For unstable waves ($k^2 + l^2 < 2\lambda^2$), the linear growth rate, $\text{Im}(\omega)$, is given by

$$\text{Im}(\omega) = |\bar{e}_k \cdot V_T| \sqrt{K^2(2\lambda^2 - K^2)/(K^2 + 2\lambda^2)}, \quad (4)$$

where the wave vector (k, l) is written in terms of a direction vector $\bar{e}_k = (k, l)/\sqrt{k^2 + l^2}$ and a magnitude $K^2 = k^2 + l^2$. We find that the direction of the wave vector of the most unstable mode is parallel to the thermal wind and maximum instability occurs for $K^2 = \sqrt{2}(\sqrt{2} - 1)$. The maximum growth rate is thus

$$\text{Im}(\omega)_{\text{max}} = |V_T| \lambda \sqrt{2}(\sqrt{2} - 1) \quad (5)$$

and it occurs for a wave which has a length scale comparable to the radius of deformation (λ^{-1}). The propagation of the most unstable mode is determined by the angle between the thermal wind and the mean wind. As we have disregarded the β -effect, we may always rotate our coordinate system such that the x -axis is in the direction of the mean wind. If we have plane

parallel, equivalent barotropic flow in the basic state, the most unstable mode will be a plane wave propagating with the mean wind. If the thermal wind is perpendicular to the mean wind, the most unstable disturbance will instead be in the form of a plane wave which is nonpropagating ($k = 0 \Rightarrow \text{Re}(\omega) = 0$). For intermediate angles, the most unstable wave will propagate with a corresponding fraction of the mean wind.

The baroclinic growth index, which we calculate as a function of the horizontal coordinates, is now defined by using the results of the previous discussion (eq. (4)),

$$\omega_i = |V_{400} - V_{700}| \lambda \sqrt{2(\sqrt{2}-1)}, \quad (6)$$

where the static stability, which enters in λ , is calculated using temperatures at 700 and 400 hPa. The same pressure levels are used to calculate the thermal wind in eq. (4). An example of the horizontal variation of ω_i is shown in Fig. 7. The baroclinic growth index has been calculated for the first guess field corresponding to the perturbation development shown in Figs. 2a–c. In Fig. 7, we see areas of enhanced baroclinic activity where the inverse growth rate ($1/\omega_i$) is less than 2 days. These areas coincide with the

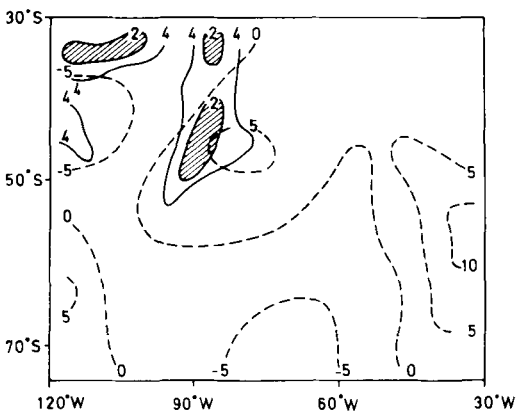


Fig. 7. Example of geographical variation of the baroclinic growth index defined in eq. (6). The flow field is given by the unperturbed initial state for the same case as in Fig. 2. Dashed curves are isolines for the 500 hPa geopotential difference field (same as Fig. 2a) while the full lines give contours of the inverse growth rate labelled in units of days. Within the hatched areas, the growth rate exceeds $\frac{1}{2} \text{ days}^{-1}$.

position of the localized perturbation in Fig. 2a, and we thus see a potential explanation for the explosive growth of the initial perturbation in the upper left hand corner of Fig. 2a. The other perturbation in Fig. 2a (lower right-hand side) which did not grow significantly in the subsequent forecast is indeed within a region of low baroclinic activity. For this particular case, it thus seems that the baroclinic growth index is a good measure of the forecast perturbation growth.

To examine if this is true in general, we have calculated an average growth index for each case in the sample which we used previously to study the RMS forecast perturbation growth. For this calculation, we use a smaller area (about $2000 \times 2000 \text{ km}^2$) centered on the position of the observation. The motivation for using a smaller area is that the regions of enhanced baroclinic activity tend to be fairly small and concentrated (see example in Fig. 2), and to avoid too much smearing out of an area of intense baroclinic activity, we average over an area which is roughly the radius of deformation. On the other hand, we must choose an area which is large enough to accommodate the perturbation introduced by the observation and its subsequent movement and growth/decay in the forecast. To minimize the movement, we now calculate the RMS difference between the 2 forecasts only at 12 h of forecast time. The baroclinic growth index is based on the flow in the 24-h forecast from the previous day which is the starting point of the unperturbed 12-h forecast. This field may also be seen as a first guess field for the analysis which included the influential observation.

We now plot the results of this correlation study in a scatter diagram (Fig. 8). Each case gives one point in the diagram, and if the perturbation growth is perfectly exponential and the average growth rate is the only factor determining the perturbation growth, all points would fall along the straight line given in Fig. 8. This is of course not the case and in fact we see a considerable scatter of the points in Fig. 8. The cloud of points is not even centered on the line and it is questionable if one can infer a tilt corresponding to the straight line from the data points. If there is no correlation at all, this implies that a baroclinic growth index has nothing to do with the growth of a perturbation in the initial state.

To obtain a more coherent picture of the structure of the data points we have processed the data further by subdividing the growth index into

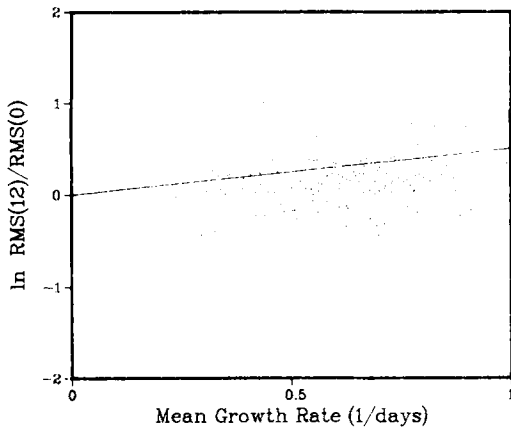


Fig. 8. Scatter diagram where one point corresponds to a particular case. The area-averaged linear growth rates and actual perturbation growths are given on the horizontal and vertical axes, respectively. If the forecast model would have followed linear theory exactly, all the points would lie on the straight line in the plot.

4 separate classes. In each class, we have computed the average and the standard deviation from the data points. The result is displayed in Fig. 9. We now see that the averages of the classes lie along a straight line whose tilt corresponds to the tilt of the ideal growth line. The vertical bars indicate the standard deviation around each point and we see that this spread is quite large. We are thus not able to say that the baroclinic growth index explains most of the computed RMS growth rates, but we can say that the baroclinic instability index gives some information on the possibility of a rapid perturbation growth. The offset of the straight line may be interpreted as an arbitrary damping factor, ω_o , i.e., assuming an exponential growth of the form $e^{(\omega_i - \omega_o)t}$ where ω_i is the area average of the growth index defined in eq. (6). The damping factor, ω_o , can be estimated by fitting a straight line to the points in Fig. 9 and noting the growth rate at the point where the straight line intersects the line $\ln[\text{RMS}(12)/\text{RMS}(0)] = 0$. In this way, we obtain $\omega_o = 0.5 \text{ days}^{-1}$, i.e., a damping time scale of 2 days. There are 2 possible physical explanations of this time scale. On the one hand, it can be interpreted as frictional damping, but the time

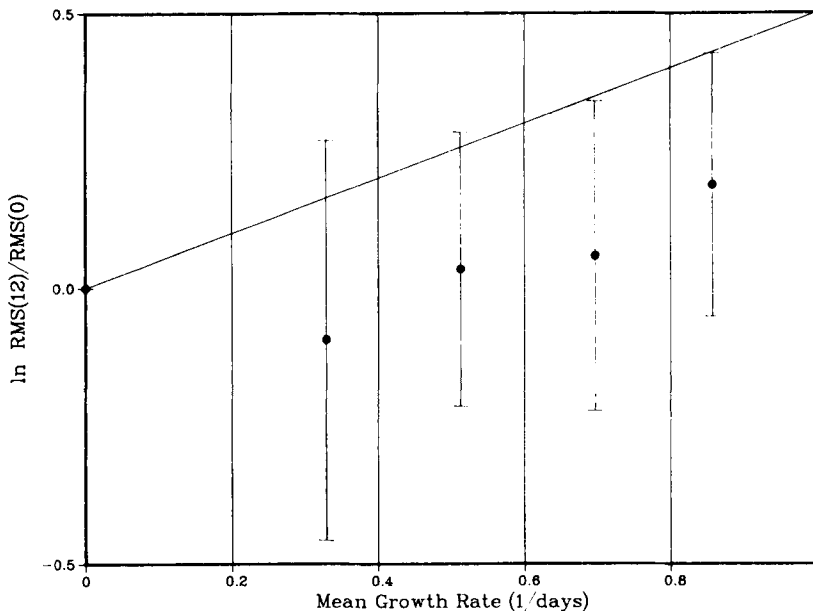


Fig. 9. Same plot as Fig. 8, but here the data points have been averaged over the classes defined by the thin vertical lines. Each dot corresponds to a class average and the standard deviation is given by the vertical bars around each dot.

scale is a bit too short for friction to be the only responsible mechanism. Another explanation is that as the perturbations arise from surface pressure observations, the initial vertical structure is essentially equivalent barotropic. It takes some time for such a disturbance to develop into an efficient, normal-mode baroclinic wave and this spin-up time acts as a damping on the system. The spin-up time is a function of the initial structure, basic state parameters, etc. (see Reinhold, 1986), and it is difficult to estimate an average value. In a study by Bengtsson (1978), the problem of baroclinic spin-up in a data assimilation cycle is treated with linear theory and he obtains a time scale of 2–3 days for typical parameter values. Furthermore, the study of Simmons and Hoskins (1979) indicates that a few days is a probable spin-up time for baroclinic waves. It thus seems that the damping factor ω_0 can be accounted for mainly in terms of a baroclinic wave spin-up time from equivalent barotropic initial conditions.

4. Barotropic error growth

Earlier studies of forecast error growth have mainly dealt with barotropic processes as being responsible for the mechanism by which perturbations may amplify. The predictability theory proposed by Lorenz (1969) and Leith and Kraichnan (1972) only deals with 2-dimensional flows and is mainly concerned with the global predictability of the flow. A more recent theory proposed by Thompson (1986) takes a local point of view of the predictability problem, but still considers the flow to be barotropic. Here, we are only interested in the localized growth problem and to examine the barotropic effects which may influence the growth of localized perturbations, we will utilize the theory suggested by Thompson (1986).

In Thompson (1986), a Green function approach is used to determine the perturbation vorticity growth in an isotropic and homogeneous basic state. It is shown that strong gradients in the basic state vorticity favour the growth of perturbation enstrophy, and an inverse growth time scale (T) may be defined

$$T^{-1} = \frac{1}{k_c} |\bar{\nabla} \zeta|, \quad (7)$$

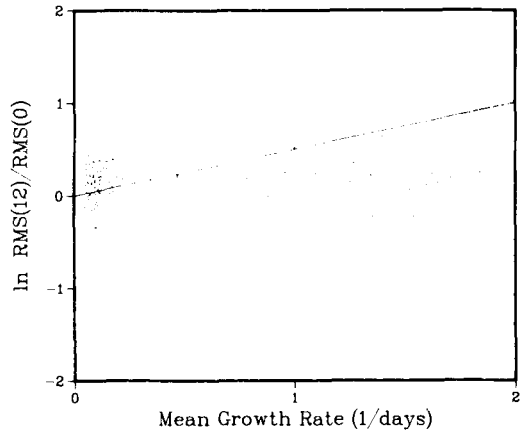


Fig. 10. Same as Fig. 8, but for the barotropic growth index given by eq. (8).

where k_c^{-1} is a characteristic length scale of the flow and the overbar denotes an average. The length scale may be taken to be the Rossby radius of deformation and we thus have a growth rate

$$T^{-1} = \lambda |\bar{\nabla} \zeta|, \quad (8)$$

where λ is the length scale parameter defined in Section 3. Proceeding as in the baroclinic case, we plot the area-averaged value of this time scale against the 12-h RMS growth factor and obtain a scatter diagram as in Fig. 10. Here there is even more scatter than in the baroclinic case and a further subdivision into growth rate classes (Fig. 11) does not reveal any well-structured relationship between the actual perturbation growth and the basic state horizontal vorticity gradients. We are thus led to the conclusion that local, barotropic processes do not seem to contribute to the perturbation growth in any systematic way.

5. Conclusions

By analysing a fairly large sample of numerical weather forecasts (152 cases) at ECMWF, we have studied the growth or decay of a localized perturbation in the initial state. The sample was selected from the routine forecasts during 4 5-month periods, 2 periods in summer and 2 periods in winter. The selection of a case was determined by the local influence of surface

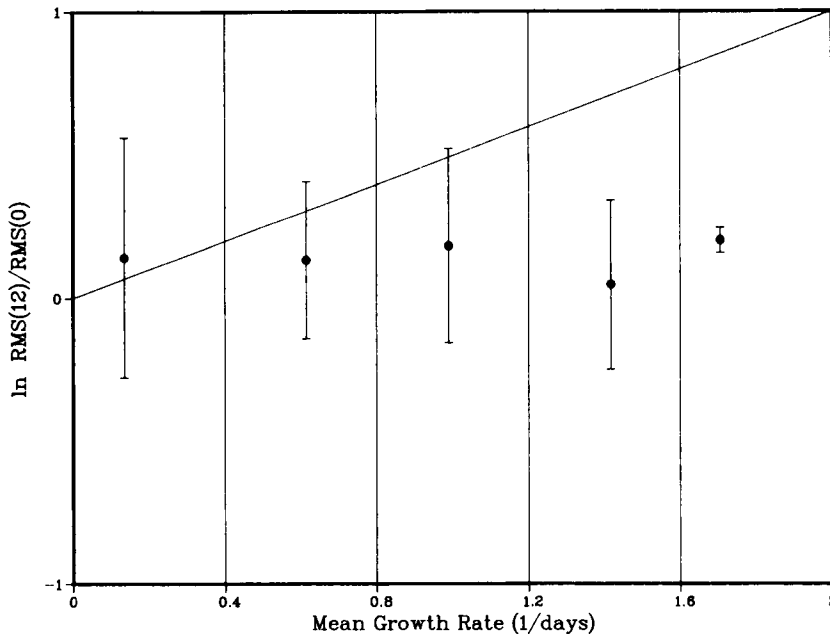


Fig. 11. Same as Fig. 9, but for the barotropic growth index given by eq. (8).

pressure observations in a data-sparse region. If such an observation had a large impact and was absent the day before, the forecast run from the day with the influential observation was compared with the forecast from the previous day. A large deviation between these 2 forecasts indicates that the localized perturbation experienced a rapid growth.

We find a very large variability in the perturbation growth and a histogram of the results indicates a bimodal distribution in the sample. Either there is very rapid perturbation growth or there is not very much happening with the initial perturbation. A possible explanation for this bimodality is that we may have localized regions in space where the "basic" flow field (in terms of the first guess field upon which the perturbation is imposed) is more sensitive to perturbations than in other places. If these regions are well localized, we may obtain a bimodal type of behaviour for a random positioning of the perturbation. We also find that there are more cases with a rapid error growth in winter than in summer. This points to the thermal gradients as being responsible for rapid perturbation growth rates.

To further shed some light on the physical processes which may be responsible for rapid perturbation growth, we have analyzed the baroclinic and barotropic flow characteristics of the first guess flow fields. We are able to find some correspondence between a rapid perturbation growth and comparatively strong thermal gradients in the basic state. There was, however, no obvious correlation between the basic state vorticity gradients and the perturbation growth as would have been expected following the ideas of Thompson (1986). This could be due to the fact that barotropic mechanisms are more effective on a longer time scale than the one considered here. By observing the center of the left-most cloud of points in Fig. 9, we see that the mean barotropic growth rate is in general very weak, implying a longer time scale.

The baroclinicity of the flow appears to be the main factor determining the impact of an isolated perturbation on a numerical weather forecast. The first guess field baroclinicity could thus be used to weight the importance of observations in an optimum interpolation analysis scheme (see Gustafson, 1981). In areas of strong baroclinicity, the first guess field should be given a small

weight relative to the observations, while in areas of weak thermal gradients, the first guess could be more relied upon. Equally important is the vertical structure of the perturbation which is introduced due to a localized observation. The perturbation growth rate is very much dependent upon the thermal advection which results. There must be a rapid energy conversion between the basic state thermal field and the perturbation velocity field and a necessary condition is that we have an optimum phase relation between the perturbation streamfunction and thermal fields (Reinhold, 1986). This aspect has not been dealt with in the present study; we have been more interested in the basic requirement for the energy conversion to take place, namely an ample supply of basic state potential energy in terms of strong thermal gradients. The basic state vorticity gradients, which could give rise to a rapid growth due to barotropic processes, do not appear to be very significant. The physical cause of this can only be

speculated upon, but it seems that the idealized barotropic growth theory suggested by Thompson (1986) is not as applicable on these time scales, as is a classical linear instability analysis for the baroclinic problem.

6. Acknowledgements

We wish to thank N. Gustafson and P. Källberg for valuable discussions and practical help with the ECMWF data retrieval system. We also thank anonymous reviewers for constructive criticism and many useful suggestions for improvements. This study was supported by NFR contracts no G-GU 1705-108 and S-FO 1705-109 and the computer resources needed to acquire the data were supplied by the Swedish Meteorological and Hydrological Institute, Norrköping, Sweden.

REFERENCES

- Arpe, K., Hollingsworth, A., Tracton, M. S., Lorenc, A. C., Uppala, S. and Källberg, P. 1985. The response of numerical weather prediction systems to FGGE level IIb data. Part II: Forecast verifications and implications for predictability. *Quart. J. R. Met. Soc.* **111**, 67–101.
- Bengtsson, L. 1978. Growth rate and vertical propagation of the initial error in baroclinic models. *Tellus* **30**, 323–334.
- Cats, G. J. 1984. Current problems in medium range forecasting at ECMWF; Data assimilation. In *Problems and prospects in long and medium range weather forecasting* (ed. D. M. Burridge and E. Källén) Berlin: Springer Verlag, 69–108.
- Dalcher, A. and Kalnay, E. 1987. Error growth and predictability in operational ECMWF forecasts. *Tellus* **39A**, 474–491.
- ECMWF, 1985. *ECMWF forecasting system documentation manual*. Data assimilation system, pp 103.
- Frederiksen, J. S. 1983. Disturbances and eddy fluxes in Northern Hemisphere flows: instability of three-dimensional January and July flows. *J. Atmos. Sci.* **40**, 836–855.
- Gustafson, N. 1981. A review of methods for objective analysis. In *Dynamic meteorology; data assimilation methods* (ed. L. Bengtsson, M. Ghil and E. Källén) New York: Springer Verlag, 17–76.
- Hollingsworth, A., Lorenc, A. C., Tracton, M. S., Arpe, K., Cats, G., Uppala, S. and Källberg, P. 1985. The response of numerical weather prediction systems to FGGE level IIb data. Part I: Analyses. *Quart. J. R. Met. Soc.* **111**, 1–66.
- Holton, J. R. 1979. *An introduction to dynamic meteorology*. Second edition. London: Academic Press, pp 391.
- Leith, C. E. and Kraichnan, R. H. 1972. Predictability of turbulent flows. *J. Atmos. Sci.* **29**, 1041–1058.
- Lorenz, E. N. 1963. The predictability of hydrodynamic flow. *Trans. N. Y. Acad. Sci. ser. II* **25**, 409–423.
- Lorenz, E. N. 1969. The predictability of a flow which possesses many scales of motion. *Tellus* **21**, 289–307.
- Lorenz, E. N. 1982. Atmospheric predictability experiments with a large numerical model. *Tellus* **34**, 505–513.
- Pierrehumbert, R. T. 1984. Local and global instability of zonally varying flow. *J. Atmos. Sci.* **41**, 2141–2162.
- Reinhold, B. B. 1986. Structural determinism of linear baroclinic waves and simple nonlinear equilibration. *J. Atmos. Sci.* **43**, 1484–1504.
- Simmons, A. J. and Hoskins, B. J. 1979. The downstream and upstream development of unstable baroclinic waves. *J. Atmos. Sci.* **36**, 1239–1254.
- Thompson, P. D. 1957. Uncertainty of initial state as a factor in the predictability of large scale atmospheric flow patterns. *Tellus* **9**, 275–295.
- Thompson, P. D. 1986. A simple approximate method of stochastic-dynamic prediction for small initial errors and short range. *Mon. Wea. Rev.* **114**, 1709–1715.